

RESEARCH ARTICLE

Analyzing the sensitivity of quantitative 3D MRI of longitudinal relaxation at very low field in Gd-doped phantoms

Danilo de Iure¹*, Allegra Conti^{1,2}, Angelo Galante^{3,4,5}, Sara Spadone¹, Ingo Hilschenz¹, Massimo Caulo^{1,6}, Stefano Sensi^{1,6}, Cosimo Del Gratta^{1,6}, Stefania Della Penna^{1,6}

1 Department of Neuroscience, Imaging and Clinical Sciences, G. D'Annunzio University of Chieti and Pescara, Chieti, CH, Italy, **2** Medical Physics Section, Department of Biomedicine and Prevention, University of Rome Tor Vergata, Rome, Italy, **3** MESVA, Department of Life, Health & Environmental Sciences, L'Aquila University, L'Aquila, AQ, Italy, **4** INFN, National Institute of Nuclear Physics, Gran Sasso National Laboratories, Assergi, L'Aquila, Italy, **5** CNR, SPIN-CNR Institute, Dept. of Physical and Chemical Sciences, L'Aquila, Italy, **6** Institute for Advanced Biomedical Technologies (ITAB), G. D'Annunzio University of Chieti and Pescara, Chieti, CH, Italy

* These authors contributed equally to this work.

* danilo.deiure@unich.it



OPEN ACCESS

Citation: de Iure D, Conti A, Galante A, Spadone S, Hilschenz I, Caulo M, et al. (2023) Analyzing the sensitivity of quantitative 3D MRI of longitudinal relaxation at very low field in Gd-doped phantoms. PLoS ONE 18(5): e0285391. <https://doi.org/10.1371/journal.pone.0285391>

Editor: Marco Giannelli, Pisa University Hospital, ITALY

Received: December 8, 2022

Accepted: April 20, 2023

Published: May 5, 2023

Peer Review History: PLOS recognizes the benefits of transparency in the peer review process; therefore, we enable the publication of all of the content of peer review and author responses alongside final, published articles. The editorial history of this article is available here: <https://doi.org/10.1371/journal.pone.0285391>

Copyright: © 2023 de Iure et al. This is an open access article distributed under the terms of the [Creative Commons Attribution License](https://creativecommons.org/licenses/by/4.0/), which permits unrestricted use, distribution, and reproduction in any medium, provided the original author and source are credited.

Data Availability Statement: Data are available from the Zenodo repository (<https://doi.org/10.5281/zenodo.7414467>).

Abstract

Purpose

Recently, new MRI systems working at magnetic field below 10 mT (Very and Ultra Low Field regime) have been developed, showing improved T_1 -contrast in projected 2D maps (i.e. images without slice selection). Moving from projected 2D to 3D maps is not trivial due to the low SNR of such devices. This work aimed to demonstrate the ability and the sensitivity of a VLF-MRI scanner operating at 8.9 mT in quantitatively obtaining 3D longitudinal relaxation rate (R_1) maps and distinguishing between voxels intensities. We used phantoms consisting of vessels doped with different Gadolinium (Gd)-based Contrast Agent (CA) concentrations, providing a set of various R_1 values. As CA, we used a commercial compound (MultiHance®, gadobenate dimeglumine) routinely used in clinical MRI.

Methods

3D R_1 maps and T_1 -weighted MR images were analysed to identify each vessel. R_1 maps were further processed by an automatic clustering analysis to evaluate the sensitivity at the single-voxel level. Results obtained at 8.9 mT were compared with commercial scanners operating at 0.2 T, 1.5 T, and 3 T.

Results

VLF R_1 maps offered a higher sensitivity in distinguishing the different CA concentrations and an improved contrast compared to higher fields. Moreover, the high sensitivity of 3D quantitative VLF-MRI allowed an effective clustering of the 3D map values, assessing their

Funding: For S.D.P., S.Sp., I.H. and C.D.G.: This work was carried out under the OXINEMS project (www.oxinems.eu), funded by the European Union's Horizon 2020 research and innovation program under Grant Agreement No. 828784. For S.D.P., C.D.G., S.Se. This work was also supported by the "Departments of Excellence 2018–2022", MIUR, for the Department of Neuroscience, Imaging and Clinical Sciences, University of Chieti-Pescara. D.d.I. was funded by the project: PON RICERCA e INNOVAZIONE 2014-2020, Dottorati innovativi a caratterizzazione industriale A.A. 2017-2018 - DOT1353282. The funders had no role in study design, data collection and analysis, decision to publish, or preparation of the manuscript.

Competing interests: The authors have declared that no competing interests exist.

reliability at the single voxel level. Conversely, in all fields, T₁-weighted images were less reliable, even at higher CA concentrations.

Conclusion

In summary, with few excitations and an isotropic voxel size of 3 mm, VLF-MRI 3D quantitative mapping showed a sensitivity better than 2.7 s⁻¹ corresponding to a concentration difference of 0.17 mM of MultiHance in copper sulfate doped water, and improved contrast compared to higher fields. Based on these results, future studies should characterize R₁ contrast at VLF, also with other CA, in the living tissues.

Introduction

In the latest years, Ultra-Low-Field (ULF, 1–100 μT) and Very-Low-Field (VLF, 1–60 mT) MRI raised the interest of the scientific community [1, 2], owing to the intrinsic advantages of the low magnetic field regime. Some of these advantages are: the compatibility with other instruments such as Magnetoencephalography (MEG) systems [3–6]; the possibility of directly imaging neural currents in cerebral regions responding to a stimulus [7, 8]; the possibility of mapping tissues' electric conductivity in brain tissues through current density imaging [9, 10]; artifact-free imaging in presence of metals, thanks to the reduced sensitivity to magnetic susceptibility [11, 12]; easier operation for specific patient populations (children, pregnant women, patients with metallic prostheses/electronic implants) [13, 14]; lower cost compared to High Field (HF, 1–3 T) devices and the possibility to implement bedside/emergency/portable setups with a considerable impact on MRI usage also in rural environments and mobile setups [1, 15]. Notably, ULF and VLF MRI scanners provide improved contrast in T₁-weighted images [16] and may represent a promising tool for investigating tumours' heterogeneity even without the use of Contrast Agents (CA), based on the intrinsic differences between the T₁ values of healthy and pathologic tissues, and the reduced signal-loss due to magnetic susceptibilities variations [11, 17].

Quantitative MRI (qMRI) provides, from a set of images, numerical information of the physical and chemical properties of tissues, such as the longitudinal and transversal relaxation rates R₁ (defined as 1/T₁) and R₂ (defined as 1/T₂), and the spin density. At high field, this technique was recently boosted thanks to the improvement in acquisition speed (see e.g. methods for MRI fingerprinting [18]). An important aspect of clinical application is the reproducibility of the results, where quantitative MRI has a clear advantage [19]. Interestingly, moving qMRI to lower fields should result in a larger dispersion of the tissues' intrinsic relaxation parameters, thus producing an improved endogenous contrast [17]. While fast 3D qMRI at 0.1 T was demonstrated [20], below 10 mT mainly 2D quantitative maps without slice selection (hereafter projected 2D mapping) were reported [2, 4, 16, 17], but the literature on 3D qMRI of longitudinal relaxation at VLF/ ULF is scant, mainly due to the poor SNR at such fields affecting the possibility of applying more time-efficient mapping sequences with a suitable spatial resolution for possible in vivo application.

To evaluate the sensitivity of our VLF MRI scanner operating at 8.9 mT [6] in quantitatively mapping physical and chemical parameters, we imaged phantoms consisting of different concentrations of a commercial Gadolinium-based CA, i.e. MultiHance® (gadobenate dimeglumine, Gd-BOPTA, 0.5 mmol/mL) in water with copper sulfate. The longitudinal relaxation rate R₁ linearly depends on the CA concentration and the relaxivity r₁. The latter depends on

various parameters [21]. Previous relaxometry studies have demonstrated the r_1 dependence of different Gadolinium-chelates on the magnetic field strength from 10 kHz to 300 MHz, including also Gd-BOPTA [22–25]. A general increase of the r_1 -values in the low frequency region is established, which should reflect in a contrast enhancement of T_1 -weighted images [26–29]. Thus, using a CA with a known relaxivity allowed us to perform a controlled analysis of the qMRI sensitivity as well as a quantitative comparison of our system and higher field ones.

To have a solid foundation to compare the different systems, we performed quantitative MRI on the same phantoms using CAs for different field strengths. To run this analysis, we compared the contrast in 3D maps of R_1 and a set of T_1 -weighted images, obtained with our VLF MRI (8.9 mT) system and clinical scanners using Low-, Standard- and High- magnetic field strengths (0.2 T, 1.5 T, and 3 T, respectively). Given that, below 20 mT, the r_1 of MultiHance was shown to be approximately constant [22], at 8.9 mT we should be operating already in the regime of maximum contrast. We thus expect an increased contrast on parametric maps and images. In addition to an analysis distinguishing the single vessels in the phantom, we assessed the sensitivity of VLF qMRI in disentangling different CA concentrations at the single voxel level through an automatic clustering over the 3D phantom maps.

Methods

Phantoms

The phantom consisted of 5 plastic vessels (cylindrical tubes with an internal diameter ~ 9 mm), with identical volumes, filled with about 1.5 ml of different solutions and placed in a piece of foam in a fixed position as depicted in Fig 1. The foam acted as a support, with dimensions fitting into the receiving coils of the MRI systems (minimum diameter ~ 80 mm). The foam's NMR signal contribution was negligible as far as we were able to tell. Four vessels were filled with different CA dilutions (MultiHance[®], Bracco, IT) in doped water (i.e. copper sulphate pentahydrate, $\text{CuSO}_4 \cdot 5\text{H}_2\text{O}$, 1000 ml H_2O , 770 mg CuSO_4 , 1 ml arquad, 0.15 ml H_2SO_4 , a commercial product by Labochimica srl, 'RAME SOLFATO Sol. Sec. Form. ml 1000'). The fifth tube contained doped water only, without CA, hereafter named the *reference* sample, with relaxation properties closer to brain tissue than pure water.

The four different Gd-dilutions in doped water were 1:3000, 1:2000, 1:1000, 1:500 with respect to the original concentration, corresponding to [0.17, 0.25, 0.5, 1] mM of MultiHance. The four concentrations were chosen to span from the highest one, corresponding to the concentration occurring in plasma right after a bolus injection of CA [30], to the lowest one, similar to the mean Gd- concentration found in muscles [31]. The longitudinal relaxation rate R_1 of each sample depends on the Gd- concentration [Gd] according to the formula:

$$R_1 = R_{1,r} + r_{1,Gd} \cdot [\text{Gd}] \quad (1)$$

valid for small concentrations [Gd], where $R_{1,r} = \frac{1}{T_{1,r}}$ is the longitudinal relaxation rate of the reference sample and $r_{1,Gd}$ is the CA relaxivity.

Recordings

MR images were recorded using four devices operating at different magnetic field strengths: a system implemented in the EU project MEGMRI, operating at 8.9 mT [6], and three commercial systems used for clinical applications operating at 0.2 T (Esote Artoscan C-Scan), 1.5 T and 3T (both Philips Achieva). The VLF system operated at a magnetic field of 8.9 mT generated by a compensated solenoid coil. A Maxwell coil generated a gradient field of 0.22 mT/

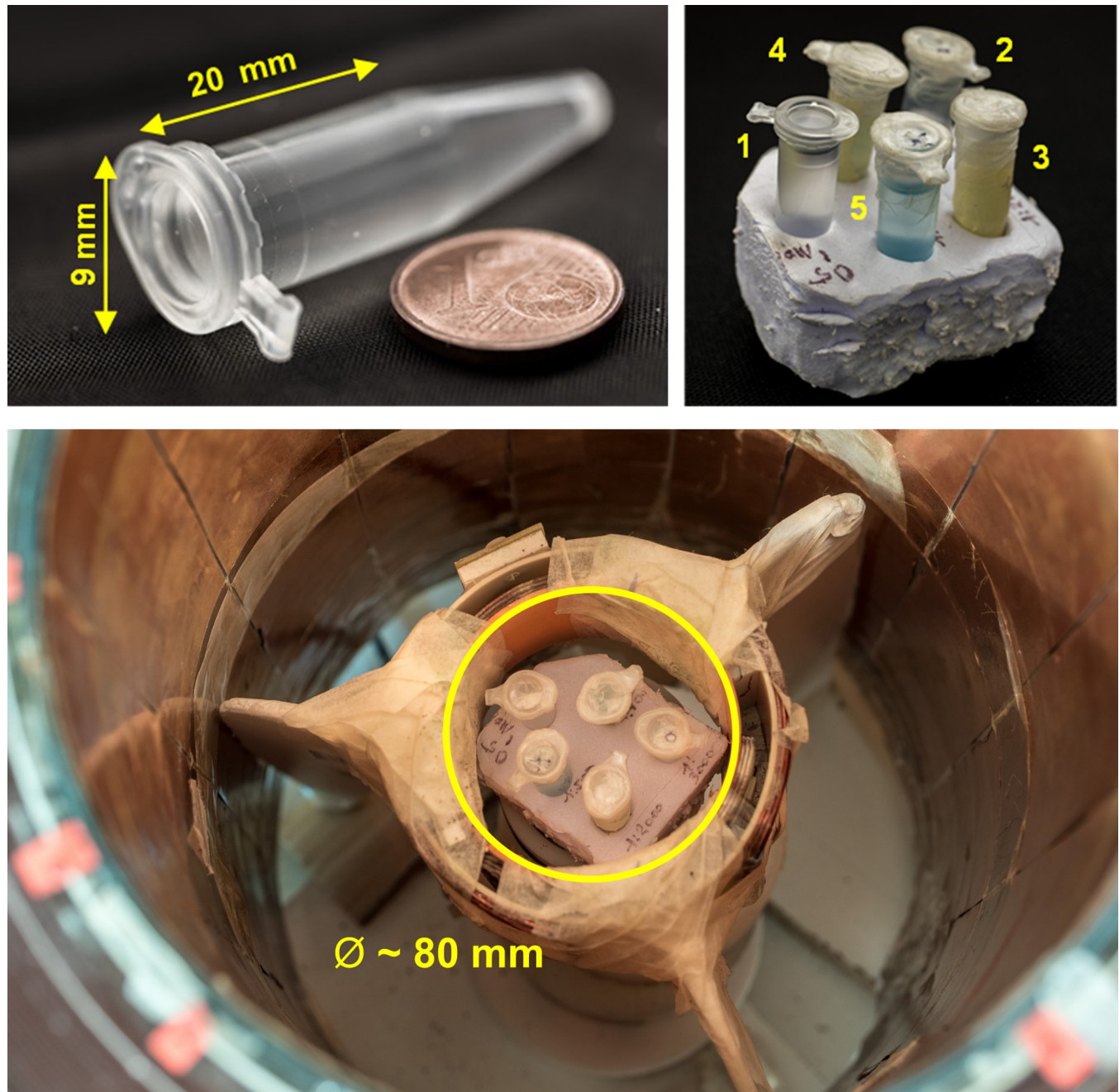


Fig 1. *Upper left:* An individual phantom vessel. *Upper right:* The 5 samples in the foam support, same positions as for the measurements. The samples are positioned as follows: 1- ref. sample, 2–0.17 mM, 3–0.25 mM, 4–0.5 mM, 5–1 mM. Each vessel is filled with about 1.5 ml of solution. *Lower:* The phantom is shown inside the VLF system.

<https://doi.org/10.1371/journal.pone.0285391.g001>

(m·A) in the Z-direction (along the solenoid axis) and the X-Y gradient coils were designed using a Finite Element method and were located on the inner surface of the solenoid generating a gradient field of 0.38 mT/(m·A). The slew-rate was approximately 5 T/(m·s). The receiver coil R_x was a saddle style coil with a diameter of 8 cm and height of 6 cm. The transmission coil T_x was placed outside the R_x coil, rotated by 90° to achieve a decoupling of around 60 dB. The Artoscan was equipped with a permanent magnet to generate the 0.2 T field and field

Table 1. MRI acquisition parameters.

	8.9 mT	0.2 T	1.5 T	3 T
Sequence	Spin-Echo 3D	Multislice Spin-Echo	Multislice Spin-Echo	Multislice Spin-Echo
T _E (ms)	19	18	8	12
T _R (ms)	[85, 100, 110, 120, 170, 250, 340, 510]	[80, 160, 240, 340, 440, 500, 740, 1000]	[160, 240, 340, 440, 500, 740, 1000]	[100, 160, 240, 340, 440, 500, 740, 1000]
FA (°)	90	90	70	70
Phase encoding steps	32x32	136	148	152
Frequency encoding steps	32	192	152	152
Voxel size (mm ³)	3.0x3.0x3.0	0.5x0.5x3.0	0.9x0.9x3.0	1.0x1.0x3.0
Min/Max Acquisition times (s)	[348, . . . , 2089]*	[220, . . . , 540]	[68, . . . , 408]	[96, . . . , 612]
Normalization	-	Mean noise	-	STD of noise

Echo Time (T_E), Recovery Time (T_R), Flip Angle (FA), spatial resolution and acquisition times at different magnetic fields. The slices in the multislice case are adjacent to each other. Noise mean and standard deviation (std) for the normalization are derived from all the voxels external to the borders identified with the segmentation algorithm.

* Please note that the 8.9 mT 3D cartesian spin-echo is not optimized, since 32 slices have to be acquired, regardless of the phantom dimensions. Conversely, at higher fields 2D multislice sequences are used.

<https://doi.org/10.1371/journal.pone.0285391.t001>

gradients of 10 mT/m with a slew rate of about 40 T/(m·s). This system was designed to image upper and lower limbs. The Philips Achieva systems were equipped with superconducting magnets and gradients of 33 mT/m and 40mT/m and slew rates 180T/(m·s) and 200 T/(m·s), respectively.

At VLF, T₁-weighted images were acquired using an isotropic 3D cartesian Spin-Echo sequence, with two phase encoding gradients and no k-space subsampling. At higher fields a cartesian multislice Spin-Echo was used with standard clinical settings, ensuring that the slice order acquisition was alternated to minimize magnetic transfer effects between adjacent slices. The k-space was under-sampled to optimize acquisition performances (according to the default suggested value from the commercial software, see [Table 1](#)) and spoiling gradients were applied at the end of each repetition to avoid spurious signal in the next one.

For each scanner, the image volume was centred, along the longitudinal direction, on the common vessels centre, and only the central slices were considered for the subsequent analysis, to avoid any edge effect contribution. At each field, images were collected for different ranges of Repetition Times (T_R), selected to span the tube relaxation functions up to at least twice the T₁ value of the reference sample. The Echo Time (T_E) was fixed at the smallest value permitted by each scanner, to minimize effects of the transversal relaxation on the signal magnitude. Finally, in each scanner, the same number of Excitations (NEX) was used, namely 4. All the acquisition parameters are summarized in [Table 1](#).

Contrast analysis on R₁ maps

The data were preprocessed as reported in the [S1 File](#) (see *Data Preprocessing* subsection). Notably, the voxel size in all the images recorded with the commercial scanners was rescaled to the VLF system. Then R₁ was estimated at each voxel by modelling and fitting the voxel signals in the masked images with the following T_R function [32]

$$S(T_R) = A \cdot (1 - e^{-T_R/T_1}) \quad (2)$$

where $A = S_0 \cdot e^{-T_E/T_2}$ is a constant depending on the transversal relaxation process, T_E is

specific for each scanner, the signal amplification was kept fixed for each set of acquisitions, and the spin density is S_0 . In this study, T_E was the lower limit allowed by each system and thus varies across systems. Eq 2 is a simplified version of a more complex formula found for repeated SE sequences [33], valid for $T_E/2 \ll T_R$ (which was always true, see Table 1) and $T_2^* \ll T_R$ [34].

The latter condition is met in our VLF setup where, during the acquisition window, the T_2^* is mainly driven by the gradient field. In fact, according to [35], field inhomogeneities affect the T_2^* as in the following:

$$\frac{1}{T_2^*} = \frac{1}{T_2} + \gamma \Delta B_{inhom} \quad (3)$$

where T_2 is the intrinsic transverse relaxation time, and ΔB_{inhom} is the magnetic field inhomogeneity across a voxel. To obtain an upper estimate of T_2^* we consider only the applied readout gradient discarding contributions from the intrinsic relaxation and the measurement field inhomogeneity. The applied sequence bandwidth is about 2.5 kHz, corresponding to 78 Hz for each of the 32 acquired voxels in the frequency direction. This results in a $T_2^* \leq 1/\gamma \Delta B_{inhom} = 13$ ms constraint, confirming the $T_2^* \ll T_R$ assumption (as the smallest T_R used in our procedure was 85 ms). The validity of this assumption was also confirmed by inspecting the signal amplitudes at the end of the acquisition window too, as reported in S1 File (see the subsection *Control measurement on the assumption $T_2^* \ll T_R$*), further solidifying the approximation.

The same held true at higher fields as well, where nulling of transverse magnetization before the excitation pulses was achieved by the inclusion of spoiling gradients. Then, for each field strength, the following steps were applied to evaluate the sensitivity to different R_1 values at the vessel level equally across different systems:

- i. R_1 values of all voxels in each vessel were analysed by 1-way ANOVA with the measurement field as a categorical factor, to evaluate possible effects of both CA concentration and field. Bonferroni's post-hoc analysis was applied to significant ($P < 0.05$) effects.
- ii. The differences between all the possible R_1 map voxel pairs of two samples with contiguous dilutions (absolute contrast) were computed for every measurement field.
- iii. The R_1 contrast values across vessel pairs were compared through 1-way ANOVA analysis over all possible voxel differences with the measurement field as a categorical factor, to evaluate possible effects of the vessel pair and the measurement field. Bonferroni's post-hoc analysis was applied to significant effects.

Contrast analysis on T_1 -weighted images

We also compared the sensitivity of the systems with spin-echo T_1 -weighted images. To account for the different T_1 values of the reference sample for each field, we selected images obtained at specific repetition times T_R^* . We first estimated the T_1 values at each field, by fitting each voxel, within the sample mask, with the function in Eq 2, and then averaged over the sample. For each measurement field, T_R^* was selected as the closest among the available T_R values, to the estimated T_1 of the reference sample. We then quantified the contrast in the T_1 -weighted images between vessel pairs using the following procedure:

- i. For each field strength, the images acquired at T_R^* were rescaled in a 0–255 scale dividing all the voxel values by the factor $\max(\text{voxels})/255$;

- ii. points (ii) to (iii) from the previous subsection *Contrast Analysis on R₁ maps* were applied to the rescaled intensities of T₁-weighted images, to evaluate pairwise contrast over the vessels in the phantom.

Clustering analysis

An automatic clustering procedure was used to determine whether, despite the low available SNR, the sensitivity of the VLF system was suitable to automatically distinguish individual voxels in the R₁ maps for different CA concentrations. The clustering procedure assigns homologous voxels to the same group, and we applied it to assess whether all the voxels in a vessel were grouped together. Voxels of the R₁ map and within the mask were clustered through a K-means procedure using a variable number of clusters (from two to nine). The optimal number of clusters (which is expected to be five) was automatically estimated through the Krzanowski-Lai criterion and maximization of the product of different clustering performance criteria [36–39]. Clustering results were evaluated in terms of accuracy in grouping voxels with the same CA concentration and in separating voxels corresponding to different CA concentrations. Specifically, for each vessel we computed the within-sample homogeneity, defined as the maximum over clusters, of the percentage of voxels in each vessel belonging to the same cluster. The percentage was referred to the total voxel number of the related vessel. Moreover, we estimated the across-samples homogeneity, defined as the percentage size of the most representative cluster of each vessel, normalized with respect to the total voxel number of the vessel, minus the related within-sample homogeneity. The last measure quantified the assignments outside the sample and in an optimal situation should be 0. Both measures were averaged across the five vessels.

Results

3D imaging of phantom at different field strengths

An example of T₁ weighted images recorded at 8.9 mT and 1.5 T is shown in Fig 2 for different T_R values. The images show the phantom comprising the reference vessel and the 4 vessels with different dilutions of MultiHance. With the same number of averages, the SNR and spatial resolution of the images recorded at VLF are lower than at higher fields. Nevertheless, it is

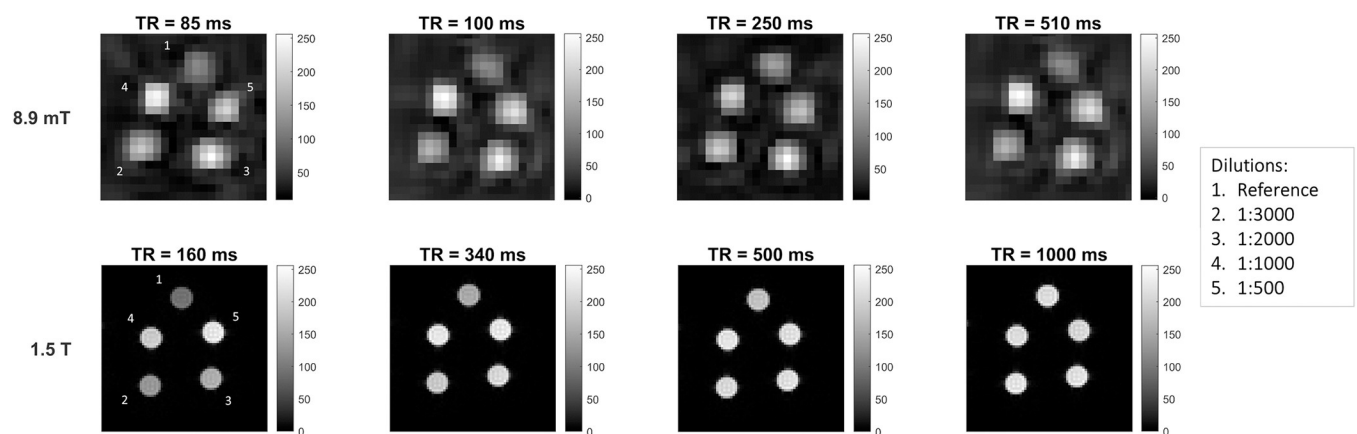


Fig 2. T₁-weighted images of the phantom. Images, at different T_R, of a central slice of a phantom composed by vessels with different MultiHance dilutions. *Upper panel:* MR images obtained at 8.9 mT. *Lower panel:* as a comparison, MR images obtained at 1.5 T.

<https://doi.org/10.1371/journal.pone.0285391.g002>

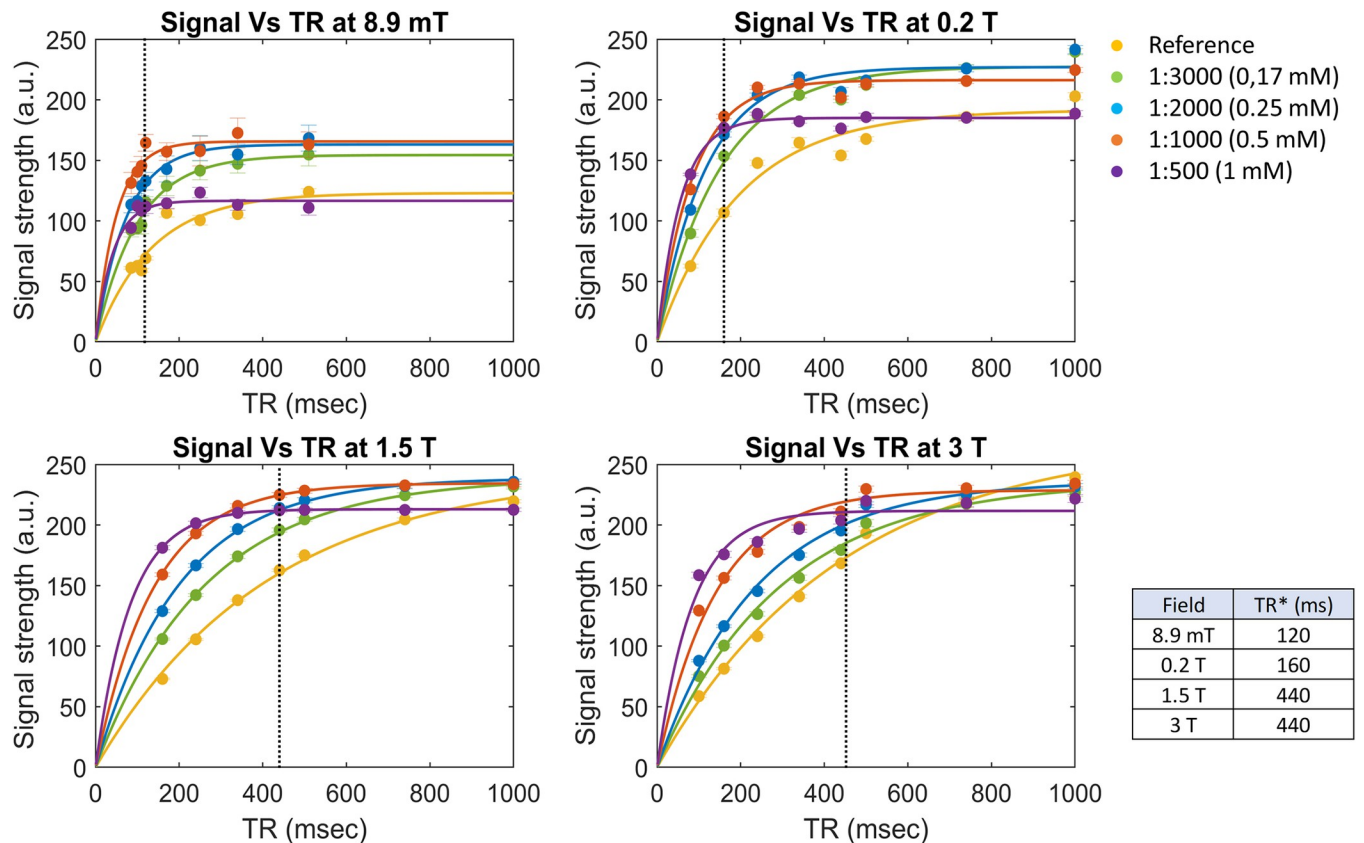


Fig 3. Mean signal over the samples. Mean signal from all the voxels of the samples at different T_R and different fields, together with the exponential fitting curve. Signals at 0.2 T and 3 T were normalized to the background noise as reported in Table 1. Error bars represent the standard error on the mean estimation. The T_R^* chosen for each field is indicated with the dotted line in each plot and reported in Table 1 for each field.

<https://doi.org/10.1371/journal.pone.0285391.g003>

still possible to identify the tubes and the differences in voxel intensities among the different CA concentrations, at least for low T_R values.

In Fig 3 we show the mean signals obtained from the central slices together with the related exponential fits according to Eq 2, we further note that in addition to the T_1 contribution, the T_2 dependence of the constant A (see Eq 2) influences the asymptotic signal values for different CA concentrations. The experimental $T_{1,r}$ values for the reference sample were about (133 ± 4) ms, (187 ± 2) ms, (413 ± 2) ms, and (445 ± 10) ms at 8.9 mT, 0.2 T, 1.5 T, and 3 T respectively (average over voxels \pm standard error). To run a quantitative comparison on image contrast, we selected the optimal T_R^* for each magnetic field among the available T_R values. The closest ones to the experimental T_1 of the reference sample were [120, 160, 440, 440] ms.

Contrast at different field strengths

T_1 -weighted images of the phantom central slice obtained at the appropriate T_R^* value for each field strength are shown in Fig 4A. Qualitatively, the difference between the reference sample and the vessels containing the Gd dilutions is clearly visible in all fields, whereas differences among the CA concentrations become more evident towards lower fields.

Fig 4B shows the corresponding R_1 -maps obtained from the masked images, including the edge voxels. In Fig 4C the same slices as in Fig 4B are shown, but after voxel resizing and edge removal for the quantitative analyses. Vessel edges were removed to avoid partial volume

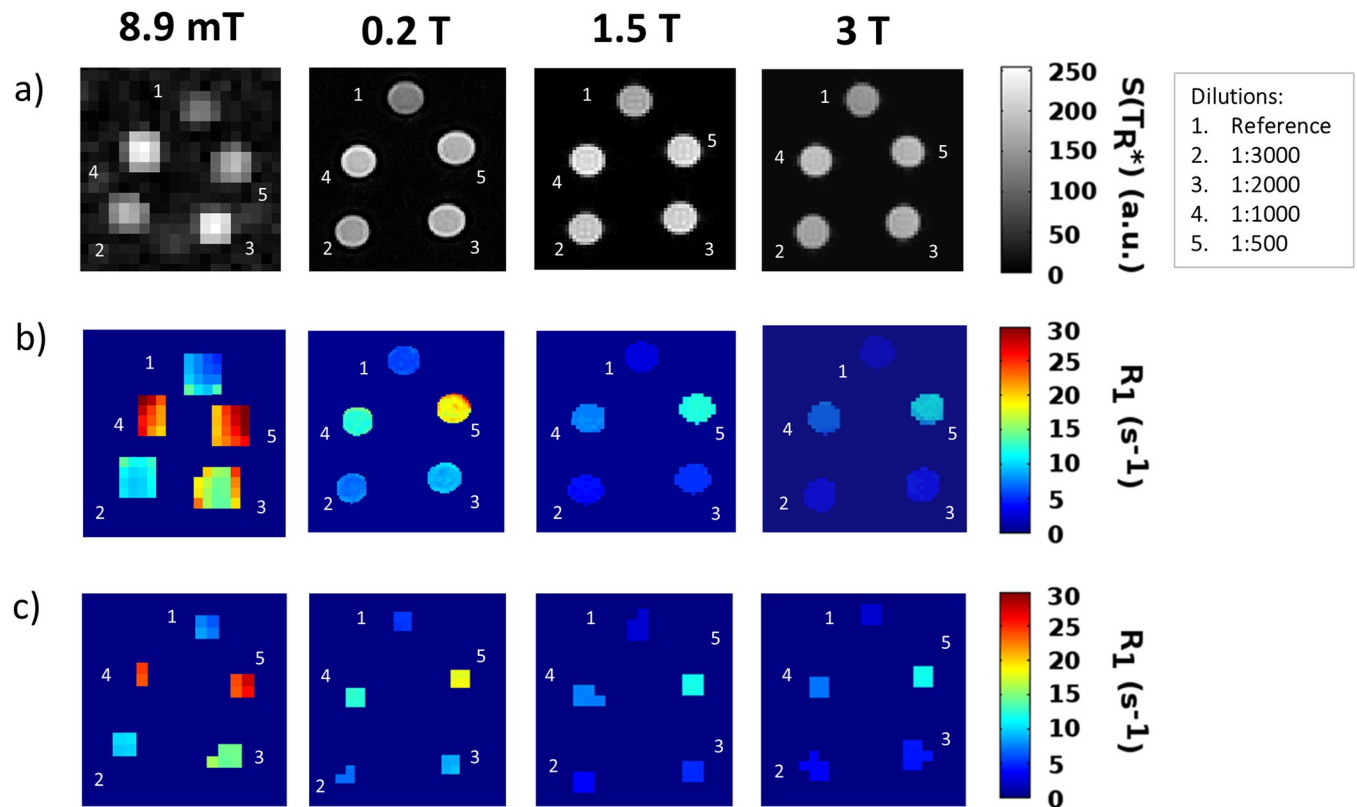


Fig 4. R₁ maps of the phantom. (a) T₁-weighted images (central slice, images at 0.2 T, 1.5 T, 3 T not resized) of the MultiHance phantom, at 8.9 mT, 0.2 T, 1.5 T and 3 T at T_R = T_R* = [120, 160, 440, 440] ms respectively. (b) R₁-maps for the same slice obtained at the same fields (no resize) by fitting the voxel signals in a mask containing the edges, as a function of T_R with the Eq 2. (c) R₁-maps from the resized images after application of the mask excluding the border voxels. These are sample slices of the actual 3D maps where the contrast and clustering analyses were performed.

<https://doi.org/10.1371/journal.pone.0285391.g004>

effects, which would include the contribution of the background noise. In the VLF regime and to a lesser extent in the other applied fields, the contrast in R₁ maps appears larger than in T₁-weighted images.

The mean R₁ values extracted from these maps for each vessel are summarized in Fig 5, where we can see the increase of the R₁ values for all the samples with decreasing field, peaking at VLF. This observation is supported by the literature reporting a longitudinal relaxivity increase at lower magnetic fields in different media [22, 24]. To quantitatively compare the R₁ values, we ran ANOVA (see S1 File for details on ANOVA results) which suggested that the vessels could be distinguished, R₁ being modulated with the measurement field as well as the CA concentration. Specifically, R₁ values at 8.9 mT were significantly larger than for the other fields and the same applies to 0.2 T versus the higher fields, while no significant differences were found between 1.5 T and 3 T. Moreover, for the VLF and the 1.5 T measurements the different vessels showed significantly different R₁ values, while it was possible to distinguish only the 3 higher CA concentrations at 0.2 T and 3 T. Finally, we fitted the estimated R₁ values reported in Fig 5, using Eq 1, obtaining the estimates of the MultiHance r₁ in doped water reported in Table 2.

Comparison between R₁ and T₁-w sensitivity at the vessel level

To highlight the improved sensitivity obtained with VLF-quantitative MRI of CA-doped vessels, we analysed through separate ANOVAs (see S1 File for details on ANOVA results) both

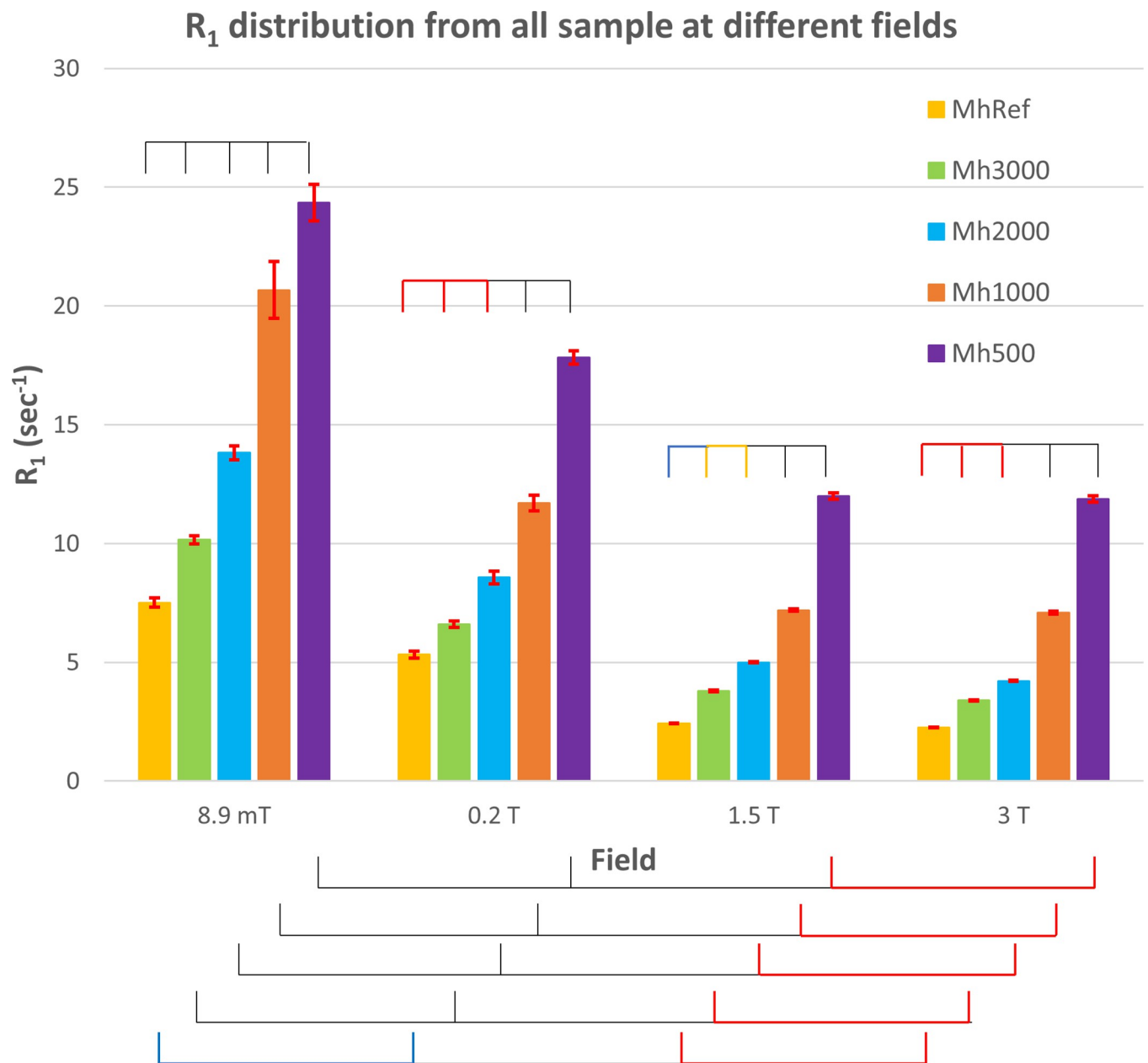


Fig 5. Histogram of the R₁ values. Mean R₁ values for each concentration and main field value with relative standard error as error bars. The mean R₁ is the average of the R₁ fitted on the single voxel of the images. Results from a 1-way ANOVA with field as categorical factor and Bonferroni correction comparison is also shown: i) spiked segments on top, over the samples at the same field indicate significant (yellow- $P < 0.03$, cyan- $P < 0.003$, black- $P < 3 \cdot 10^{-7}$) and not significant (red) comparisons over subsequent CA concentrations. The reference sample is compared to the lower CA concentration. ii) spiked segments in the bottom indicate significant and not significant comparisons (same notation as above) of the same sample tube across the scanners.

<https://doi.org/10.1371/journal.pone.0285391.g005>

the differences between R₁ values (R₁ contrast) and then, as a comparison, the ones between the normalized signals (signal contrast) obtained from the phantom vessels across the measurement fields. The normalization of the T₁-weighted images on the 0–255 scale allowed a direct comparison of performances at different field strengths.

The bar plot in Fig 6 shows the inter-vessels spreads of the R₁ (Fig 6 left) and the normalized T₁-weighted variations (Fig 6 right) between the higher Gd concentration (Mh500) and the reference sample for all magnetic field strengths.

Table 2. r_1 relaxivities.

	8.9 mT	0.2 T	1.5 T	3T
MultiHance r_1 (mM·s) ⁻¹	17.3	12.7	9.6	9.8
Fit error (mM·s) ⁻¹	3	0.4	0.1	0.3

Relaxivity of MultiHance in water doped with copper sulfate and the related estimation error.

<https://doi.org/10.1371/journal.pone.0285391.t002>

ANOVA confirmed that R_1 contrast is significantly larger as the field decreases. Notably, such an increase is not that clear in the T_1 -weighted image differences, where it seems that the maximum contrast is obtained at 0.2 T, and then decreases with the increasing field. These results suggest that R_1 maps at VLF are more reliable than T_1 -weighted images, due to their higher SNR and the lack of T_2 effects which instead affect the T_1 -weighted images.

In Fig 7 upper we show the R_1 contrast between pairs of samples with contiguous Gd dilutions, together with the normalized T_1 -weighted voxel value contrast (Fig 7 lower). Qualitatively, the R_1 contrast is always positive, in all fields. However, from the ANOVA interaction reported in Fig 5, only at 8.9 mT and 1.5 T all the R_1 contrasts were significantly different from zero, while only contrasts between higher concentrations were different from zero at 0.2 T and 3 T. In general, the R_1 contrast seems to increase as the measurement field decreases, as confirmed by 1-way ANOVA with the field as the categorical factor, and no significant differences were found between 1.5 T and 3 T. R_1 contrast was also significantly larger as the CA concentration increased, and this increase was enhanced by the decreasing field, except for the highest CA concentration at VLF. This effect was possibly induced by inadequate sampling in the low T_R range (see Discussion). Notably, in the other fields, the contrast of Mh3000 vs the reference sample and Mh2000 vs Mh3000 did not differ as at VLF (we even note a significant decrease at 3 T), suggesting an increased sensitivity in the VLF setup to differences in low CA concentrations, consistently with results shown in Fig 5. The contrast at higher CA concentration is instead clearly detectable. When comparing the contrast across the fields we obtained that, except for the contrast between the higher CA concentrations (Mh500-Mh1000), all the other

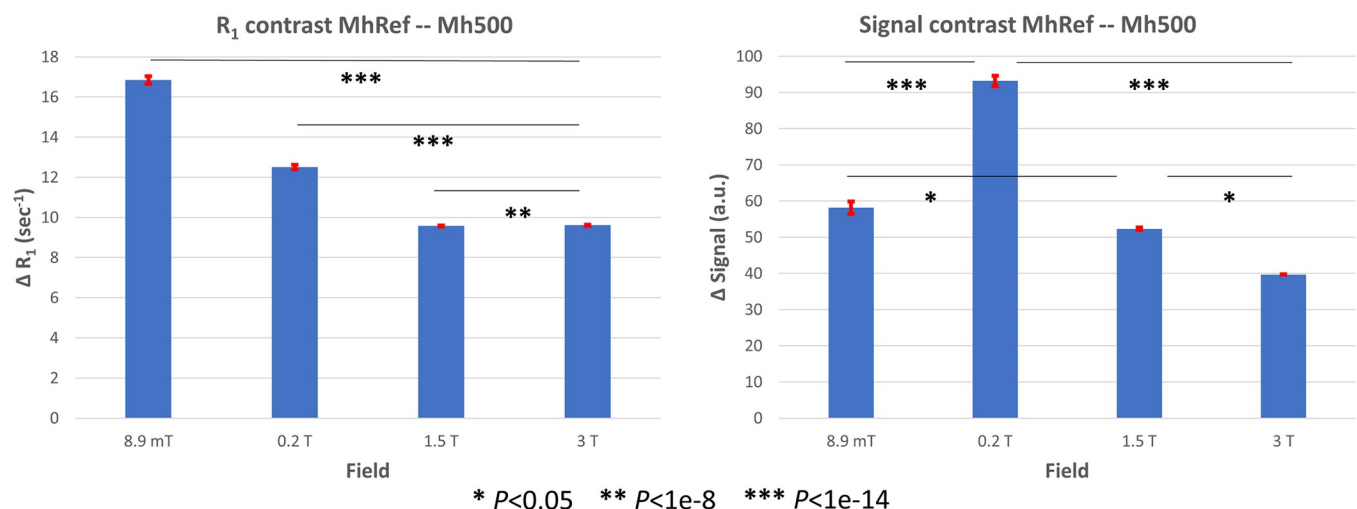


Fig 6. Contrasts between the extremal dilutions. *Left:* Relaxation rate contrast between the reference sample and the sample with the lowest dilution (1:500); *Right:* Analogous analysis to the previous one but on the distributions of the differences between the normalized voxel intensities over the T_1 -weighted images. Significant comparisons are reported on the bar plot. For R_1 values, contrast is strongly enhanced at VLF. For images, the contrast enhancement is not clear, probably due to the poor SNR in the VLF images and to T_2 effects.

<https://doi.org/10.1371/journal.pone.0285391.g006>

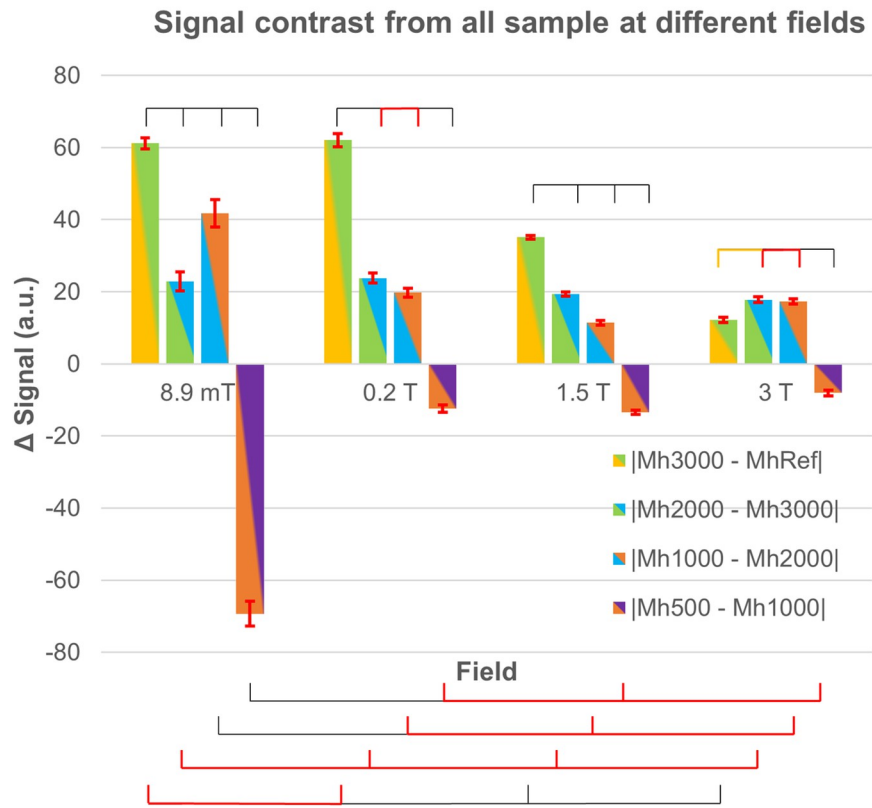
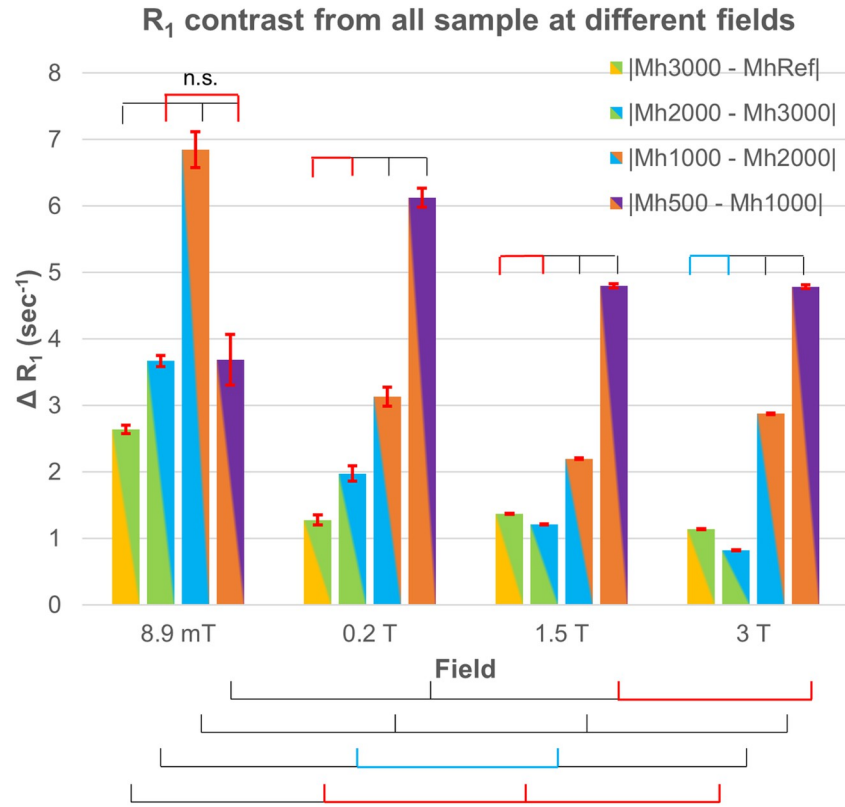


Fig 7. Contrasts between close dilutions. *Upper:* R_1 contrast between samples with contiguous CA dilutions at different fields. The lower dilution was compared to the reference sample. *Lower:* T_1 -weighted normalized signal contrast, for $T_R = T_R^*$ at each field, between the same sample pairs. The contrast between the higher CA concentrations is negative at all the measurement fields and is larger at 8.9 mT possibly due to T_2 effects enhanced at VLF.

<https://doi.org/10.1371/journal.pone.0285391.g007>

contrasts were always larger at VLF than at the other fields (see [Discussion](#)). In summary, with $NEX = 4$ at VLF we could clearly detect the smaller contrast in our phantom, which was 2.7 s^{-1} , corresponding to a concentration of 0.17 mM of gadobenate dimeglumine in copper sulfate doped water.

As a comparison, we show in [Fig 7 lower](#) the normalized T_1 -weighted signal contrast estimated at the T_R^* for each field. First, we note that the contrast between the 2 higher CA concentrations is negative (it is significantly different from zero only at VLF), but this, as further discussed later, is due to T_2 effects. At VLF, all the other contrasts are significantly different from zero, whereas only the first contrast is significantly different from zero at 0.2 T and 1.5 T and none at 3 T.

The mean R_1 (signal) contrast is the average of all the possible R_1 (signal) differences over single voxels pairs comprised in the mask and included in two samples with contiguous CA dilutions. Results from a 1-way ANOVA with field as categorical factor and Bonferroni correction comparison is also shown: i) spiked segments on top, over the samples at the same field indicate significant (orange- $P < 0.03$, cyan- $P < 0.003$, black- $P < 3 \cdot 10^{-7}$) and not significant (red) comparisons over subsequent contrasts; ii) spiked segments in the bottom indicate significant and not significant comparisons (same notation as above) of the same sample tube across the scanners.

Clustering analysis

Finally, we inspected the sensitivity of VLF R_1 3D mapping for single voxels, using a clustering algorithm to automatically assign each voxel to a vessel. The results of the clustering procedure are shown in [Fig 8](#). Notably, the algorithm automatically identified five clusters. Four clusters identified four different vessels (the reference sample–yellow–, the two lower CA concentrations–green and cyan–and the higher CA concentration–violet) except for a few edge voxels. The identification of the Mh1000 sample was not as clear as for the other samples, instead this sample appeared split into two clusters in the upper and lower part along the axial axis. The voxels in the upper part were assigned to the violet cluster, whereas the ones in the lower part were assigned to the fifth cluster, the orange one. The average within-samples homogeneity was 87.5%. Moreover, the grouping error, i.e. the assignments outside the sample quantified through the corresponding average across-sample homogeneity, was 11.7%. These values of the within-samples and the across-samples homogeneity estimated over all the clusters confirmed the capability of VLF R_1 maps to distinguish voxels corresponding to different CA concentrations. For the Mh1000 sample, the accuracy decreased to 57%, while the across-sample homogeneity for the violet and orange cluster was 23% and 28% respectively. For this sample, the grouping error is induced by the higher dispersion of the R_1 values. The average across-sample homogeneity was also affected by some edge voxels in other clusters, due to the partial volume effect (see [Discussion](#)), induced by the large voxel size. Overall, these results confirm an R_1 sensitivity value better than 2.7 s^{-1} , even at the single voxel level with 3 mm side.

Discussion

In this work, we evaluated the sensitivity of R_1 maps and 3D T_1 -weighted images obtained with an in-house MRI setup operating at 8.9 mT using a phantom consisting of different CA

Clustering on the 3D volume

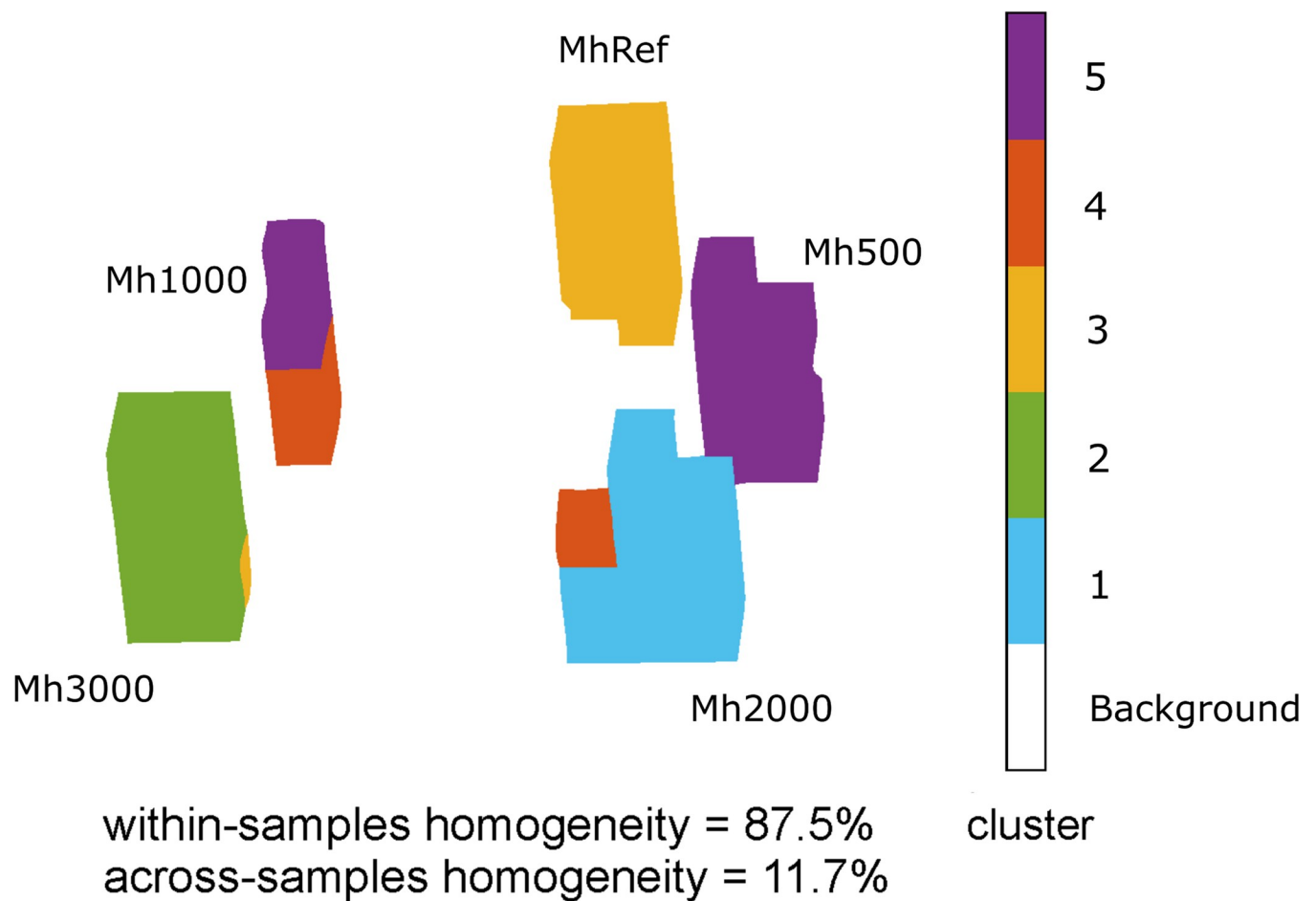


Fig 8. Clustering results on the 8.9 mT R₁ maps. Optimal clusters number are obtained through a mixed performance criterion (see [Methods](#)). Cluster colour and numbering are consistent across clustering types. Homogeneity values reported below each cluster show that voxels are in general grouped according to the CA dilution. Grouping over the two samples at higher CA concentration is less homogenous, due to effects of inadequate sampling at low T_R.

<https://doi.org/10.1371/journal.pone.0285391.g008>

concentrations in doped water. For comparison, similar results were also obtained by three other commercial scanners operating at higher fields and used for routine clinical investigation, a system at 0.2 T, 1.5 T, and 3 T. We quantitatively analysed the R₁ maps, demonstrating that at VLF we could distinguish the samples and even the voxels at different CA concentrations (as assessed through the automatic clustering). Conversely, the lower CA dilutions could not be separated at higher fields. Moreover, the contrast in R₁ maps was, in general, higher at VLF than at the other fields, and increased with the CA concentration, while unclear contrast patterns were obtained when inspecting contrast on normalized T₁-weighted images. Overall, we assessed the possibility of quantitative 3D mapping at VLF, able to distinguish different CA concentrations in a clinical-relevant interval, even with the low SNR and spatial resolution at this field, and to provide more sensitive and clear results than T₁-weighted image contrast, at least at the sample or voxel group level.

Methodological considerations on R₁ mapping of CA concentration at VLF

A clear result obtained with our VLF MRI system is that the sensitivity of the instrument is suitable to distinguish different CA concentrations in doped water (see Fig 5), even for single voxels which were grouped consistently within the sample they belonged to (see Fig 8). On one side we expect that R₁ increases for all the concentrations when lowering the measurement field, thus making it easier to distinguish the different concentrations. Relaxometry measurements on commonly used Gd-based contrast agents showed r₁ values higher at ULF/VLF than at higher field strengths [22, 40]. For MultiHance in water, the transition from low to high values occurs in the frequency interval from 5 to 20 MHz, which is above the resonance frequency of our VLF system (375 kHz), includes the 0.2 T scanner and is below the frequencies of the other two scanners. Although this explains why we expect R₁ maps at VLF to be more sensitive than in larger fields, ULF/VLF still suffers from poor SNR and limited voxel resolution, and its ability to distinguish different CA concentrations was a challenge. However, R₁ maps were more robust than if utilising the signal intensity images. This increases the reliability of R₁ maps, as assessed by the clustering results, where even single voxels were correctly assigned to the related sample. Given that T₁ of biological tissues should scale with the measurement field (see [17]), increasing contrast, these results are promising in the perspective of in vivo R₁ mapping at VLF, also supported by CAs administration.

Instead, interpreting 3D T₁-weighted images is more difficult. First, these images suffer from the background noise, which is higher at lower fields and when a small number of averages is used to speed up the recordings. Second, the reduction of T₂ at the higher CA concentrations affects the signal intensity and in particular its asymptotic values (see Fig 3 and the coefficient A in Eq 2), making it difficult to interpret the T₁-weighted images as in the case of Mh500-Mh1000 in Fig 7 lower, where the contrast between these two samples changes polarity compared to the other contrasts. Similar effects are also shown in Fig 6 right, where a clear trend of image contrast as a function of the measurement field is not found, even when the highest concentration and the reference sample are compared. Notably, R₁ maps do not suffer from these confounds and thus the contrast trend is in general clearer, with an overall increase at VLF compared to the other fields together with an increase with the CA concentration.

Limitations of R₁ mapping at VLF

We have to acknowledge a few limitations for R₁ mapping at VLF, which however could be solved in future implementations. The first limitation deals with effects of large R₁ and explains the results obtained at VLF on R₁ contrast for the higher CA concentrations, and consequently on the clustering at the single voxel level. Specifically, despite the Mh500-Mh1000 R₁ difference being significantly larger than zero, it was not as large as expected from the other contrasts trend, while the Mh1000-Mh2000 was larger than expected. This is due to an increase of the error in the estimation of R₁ possibly affecting the higher CA concentrations, which was unavoidable with our VLF MRI spectrometer, since the current console did not allow to use T_R values below 85 ms. This led to a sub-optimal sampling for the higher CA concentrations, where T₁ was considerably shortened, thus increasing the fit error. This effect also explains the suboptimal grouping for the sample Mh1000, in the 3D clustering (the orange/violet sample in Fig 8).

The second limitation is the low SNR of VLF imaging, affecting the attainable image resolution and recording time. Here we decided not to compensate SNR with averages, using the same number of excitations (NEX = 4) for all the setups, to limit the acquisition time. In this condition, since the SNR scales as B₀^{7/4} in the low frequency coil-dominated noise regime, VLF imaging suffers from a poor SNR compared to higher fields. This limits, the spatial

resolution to a voxel size of $3 \times 3 \times 3 \text{ mm}^3$, since the SNR linearly scales with the voxel volume and higher spatial resolution would result in unacceptable acquisition time. This resolution allows 3D imaging but mis-shapes the sample geometry (the tube's section does not appear to be circular). Notably, for all the across-field comparisons shown in Figs 5 to 7, we used the same resolution also for the higher field images. This further affected the performance of the algorithms near, or on, the edges where we couldn't completely eliminate the partial volume effect due to instabilities in the R₁ fitting because of low SNR. This reflects in the clustering instability of a few peripheral voxels even after edge erosion (see the few voxels which were incorrectly grouped in Fig 8), reducing the within-sample homogeneity and affecting the single-voxel sensitivity. This effect could in principle be reduced by increasing the SNR and reducing the voxel size, dramatically increasing the recording time. In the present work, the recording time was long but the sequence we used was not optimized for fast imaging, which still has to be implemented.

Especially for in-vivo measurements these limitations have multiple implications. The long recording times and the lower specificity for low T₁ times can be remedied by optimising the current sequence parameters or moving to other more efficient approaches like 2D multislice or alternative quantitative sequence designs [18, 19]. This however was impossible with the available hardware at the time. The lower SNR of VLF and thus the best spatial resolution, which is still suboptimal for in-vivo imaging, have further reaching restrictions, which are inherently fixed by the measurement field, limiting better single-voxel sensitivity and clustering accuracy. Improvements could be made by further optimising the existing hardware like the RF coils, amplifiers for lower noise floors, or the implementation of intermediate sensors to boost the signal strength [5]. Also, Artificial Intelligence techniques applied in the novel VLF systems operating at 50–60 mT [1, 15] should be tested at this lower field and SNR regime. We believe that a combination of these efforts should be promising to enable in-vivo measurements or at least boost the capability of VLF MRI making it a suitable alternative. It is important to note that even if with longer recording times and lower SNR and resolution, this technique could provide novel information on relaxation rates, which are not available with standard clinical setups at higher fields.

Conclusion

The advantage of T₁ contrast in ULF MRI was already discussed some years ago for phantoms, showing T₁-weighted images of agarose gel [26, 41]. Projected 2D T₁ mapping demonstrated the potentiality of this technique in distinguishing different concentrations of MnCl₂, within a range of R₁ values similar to the one considered in this work [42]. Projected 2D T₁ mapping was also applied to different tissue types in ex-vivo prostate tumours and in the healthy brain [16, 17] 3D qMRI was then demonstrated in security applications, but with a voxel size considerably larger than in our case [43]. Our results extend these works, as we demonstrated the feasibility of 3D R₁ mapping at VLF with a sensitivity better than 2.7 s^{-1} and a spatial resolution of 3 mm. This result is supported by statistical and clustering analysis showing that voxels within the samples were correctly grouped and distinguished, even for small CA concentration differences. This represents a clear advantage of 3D R₁ mapping compared to T₁-weighted images at VLF, since the latter did not produce reliable results and a robust distinction among different samples was not possible, especially for low CA concentrations. All these results are promising in the perspective of a factual application of 3D R₁ mapping at VLF for in vivo recordings.

Our research also provides information on 3D VLF MRI with Gd-based CA, complementing the findings on projected 2D T₁ mapping at ULF MRI through comparison with higher fields [42]. As shown in Figs 5 and 8, the lower CA concentrations were clearly separated and

distinguishable from the reference sample while at higher fields this was possible only for the higher CA concentrations. These results could be a good resource on applications of Gd-based CA at VLF in clinics, especially with deployment of recent 50–60 mT clinical systems (Swoop [15]). Of course, the future evolution of our findings will be VLF 3D quantitative mapping in other media and in tissues, to verify its effectiveness. The field-dependent behaviour of several CAs relaxometry parameters, showing r_1 enhancement at lower fields, can draw the wrong conclusion that effortless lesion contrast enhancement can be obtained by reducing the main magnetic field. This is not always true since CA relaxivity, as well as the tissue contrast before CA administration, both determine the final contrast after CA administration. At low fields, the former is often larger, but the latter is reduced by the inherently shorter tissue relaxation times.

Finally, it is worth noting that evidence is available of remarkable low-field performances of non-Gd-based CAs like Superparamagnetic Iron Oxide Nanoparticles (SPIONs, acting mostly on the transversal relaxation times). If the low-to-high field relaxivity ratio of Gd complexes generally is up to one order of magnitude, SPIONs can reach up to two orders of magnitude thus boosting the relaxivity effect on the final tissue contrast [44]. Thus, future studies should feature more CAs, still compared at different magnetic field strengths but use the same timing sequences wherever possible.

Supporting information

S1 File. Additional information. Additional details on data pre-processing, working assumptions and ANOVA results.
(DOCX)

Author Contributions

Conceptualization: Allegra Conti, Angelo Galante, Massimo Caulo, Stefano Sensi, Cosimo Del Gratta, Stefania Della Penna.

Formal analysis: Danilo de Iure, Sara Spadone, Stefania Della Penna.

Funding acquisition: Stefano Sensi, Stefania Della Penna.

Investigation: Allegra Conti.

Methodology: Danilo de Iure, Sara Spadone, Ingo Hilschenz, Stefania Della Penna.

Software: Danilo de Iure, Sara Spadone.

Supervision: Stefania Della Penna.

Writing – original draft: Danilo de Iure, Allegra Conti, Stefania Della Penna.

Writing – review & editing: Angelo Galante, Ingo Hilschenz, Massimo Caulo, Stefano Sensi, Cosimo Del Gratta.

References

1. Liu Y, Leong ATL, Zhao Y, Xiao L, Mak HKF, Tsang ACO, et al. A low-cost and shielding-free ultra-low-field brain MRI scanner. *Nature Communications*. 2021 December; 12. <https://doi.org/10.1038/s41467-021-27317-1> PMID: 34907181
2. Sarracanie M, Salameh N. Low-Field MRI: How Low Can We Go? A Fresh View on an Old Debate. *Frontiers in Physics*. 2020; v.

3. Magnelind PE, Gomez JJ, Matlashov AN, Owens T, Sandin JH, Volegov PL, et al. Co-registration of interleaved MEG and ULF MRI using a 7 channel low-T c SQUID system. *IEEE Transactions on Applied Superconductivity*. 2011; 21(3 PART 1): p. 456–460.
4. Vesanen PT, Nieminen JO, Zevenhoven KCJ, Dabek J, Parkkonen LT, Zhdanov AV, et al. Hybrid ultra-low-field MRI and magnetoencephalography system based on a commercial whole-head neuromagnetometer. *Magnetic Resonance in Medicine*. 2013; 69(6): p. 1795–1804. <https://doi.org/10.1002/mrm.24413> PMID: 22807201
5. Sinibaldi R, De Luca C, Nieminen JO, Galante A, Pizzella V, Sebastiani P, et al. NMR detection at 8.9 mT with a GMR based sensor coupled to a superconducting Nb flux transformer. *Progress In Electromagnetics Research*. 2013; 142.
6. Galante A, Sinibaldi R, Conti A, De Luca C, Catallo N, Sebastiani P, et al. Fast room temperature very low field-magnetic resonance imaging system compatible with magnetoencephalography environment. *PLoS One*. 2015; 10: p. e0142701. <https://doi.org/10.1371/journal.pone.0142701> PMID: 26630172
7. Körber R, Nieminen JO, Höfner N, Jazbinšek V, Scheer HJ, Kim K, et al. An advanced phantom study assessing the feasibility of neuronal current imaging by ultra-low-field NMR. *Journal of Magnetic Resonance*. 2013; 237: p. 182–190. <https://doi.org/10.1016/j.jmr.2013.10.011> PMID: 24252245
8. Höfner N, Storm JH, Hömmen P, Cassarà AM, Körber R. Computational and Phantom-Based Feasibility Study of 3D dcNCl With Ultra-Low-Field MRI. *Frontiers in Physics*. 2021; 9.
9. Vesanen PT, Nieminen JO, Zevenhoven KCJ, Hsu YC, Ilmoniemi RJ. Current-density imaging using ultra-low-field MRI with zero-field encoding. *Magnetic Resonance Imaging*. 2014; 32: p. 766–770. <https://doi.org/10.1016/j.mri.2014.01.012> PMID: 24731792
10. Körber R, Kieler O, Hömmen P, Höfner N, Storm JH. Ultra-sensitive SQUID systems for applications in biomagnetism and ultra-low field MRI. In 2019 IEEE International Superconductive Electronics Conference (ISEC); 2019. p. 1–3.
11. Kraus RH, Espy M, Magnelind P, Volegov PL. Ultra-low field nuclear magnetic resonance: a new MRI regime: Oxford University Press; 2014.
12. Möble M, Han SI, Myers WR, Lee SK, Kelso N, Hatridge M, et al. SQUID-detected microtesla MRI in the presence of metal. *Journal of Magnetic Resonance*. 2006; 179: p. 146–151. <https://doi.org/10.1016/j.jmr.2005.11.005> PMID: 16310385
13. Wilde JPD, Rivers AW, Price DL. A review of the current use of magnetic resonance imaging in pregnancy and safety implications for the fetus. *Progress in Biophysics and Molecular Biology*. 2005; 87: p. 335–353. <https://doi.org/10.1016/j.pbiomolbio.2004.08.010> PMID: 15556670
14. Schukro C, Puchner SB. Safety and efficiency of low-field magnetic resonance imaging in patients with cardiac rhythm management devices. *European Journal of Radiology*. 2019; 118: p. 96–100. <https://doi.org/10.1016/j.ejrad.2019.07.005> PMID: 31439265
15. Deoni S, Medeiros P, Deoni A, Burton P, Beauchemin J, D'sa V, et al. Development of a mobile low-field MRI scanner. *Scientific Reports*. 2022 April 5; 12: p. 5690. <https://doi.org/10.1038/s41598-022-09760-2> PMID: 35383255
16. Inglis B, Buckenmaier K, Sangiorgio P, Pedersen A, Nichols M, Clarke J. MRI of the human brain at 130 microtesla. *Proceedings of the National Academy of Sciences*. 2013 November 19; 110: p. 19194–19201.
17. Busch S, Hatridge M, Möble M, Myers W, Wong T, Mück M, et al. Measurements of T1-relaxation in ex vivo prostate tissue at 132 μ T. *Magnetic Resonance in Medicine*. 2012; 67: p. 1138–1145.
18. Ma D, Gulani V, Seiberlich N, Liu K, Sunshine JL, Duerk JL, et al. Magnetic resonance fingerprinting. *Nature*. 2013 March; 495: p. 187–192. <https://doi.org/10.1038/nature11971> PMID: 23486058
19. Gulani V, Seiberlich N. Quantitative MRI: Rationale and Challenges. In *Advances in Magnetic Resonance Technology and Applications*. Elsevier; 2020. p. xxxvii–li.
20. Ayde R, Senft T, Salameh N, Sarracanie N. Deep learning for fast low-field MRI acquisitions. *Sci Rep*. 2022 Jul 6; 12(11394). <https://doi.org/10.1038/s41598-022-14039-7> PMID: 35794175
21. Caravan P. Strategies for increasing the sensitivity of gadolinium based MRI contrast agents. *Chemical Society Reviews*. 2006; 35: p. 512–523. <https://doi.org/10.1039/b510982p> PMID: 16729145
22. Laurent S, Elst LV, Muller RN. Comparative study of the physicochemical properties of six clinical low molecular weight gadolinium contrast agents. *Contrast media & molecular imaging*. 2006; 1: p. 128–137. <https://doi.org/10.1002/cmml.100> PMID: 17193689
23. Rinck PA, Muller RN. Field strength and dose dependence of contrast enhancement by gadolinium-based MR contrast agents. *European radiology*. 1999; 9: p. 998–1004. <https://doi.org/10.1007/s003300050781> PMID: 10370005

24. Rohrer M, Bauer H, Mintorovitch J, Requardt M, Weinmann HJ. Comparison of magnetic properties of MRI contrast media solutions at different magnetic field strengths. *Investigative radiology*. 2005; 40: p. 715–724. <https://doi.org/10.1097/01.rli.0000184756.66360.d3> PMID: 16230904
25. Caravan P, Farrar CT, Frullano L, Uppal R. Influence of molecular parameters and increasing magnetic field strength on relaxivity of gadolinium- and manganese-based T1 contrast agents. *Contrast Media & Molecular Imaging*. 2009; 4: p. 89–100. <https://doi.org/10.1002/cmml.267> PMID: 19177472
26. Lee SK, Mo M, Myers W, Kelso N, Trabesinger AH, Pines A, et al. SQUID-detected MRI at 132 μ T with T1-weighted contrast established at 10 μ T–300 mT. *Magnetic Resonance in Medicine*. 2005; 53(1): p. 9–14.
27. Macovski A, Conolly S. Novel approaches to low-cost MRI. *Magnetic resonance in medicine*. 1993; 30: p. 221–230. <https://doi.org/10.1002/mrm.1910300211> PMID: 8366803
28. Stepišnik J, Eržen V, Kos M. NMR imaging in the earth's magnetic field. *Magnetic resonance in medicine*. 1990; 15: p. 386–391. <https://doi.org/10.1002/mrm.1910150305> PMID: 2233218
29. Seton HC, Hutchison JMS, Bussell DM. A 4.2 K receiver coil and SQUID amplifier used to improve the SNR of low-field magnetic resonance images of the human arm. *Measurement Science and Technology*. 1997; 8: p. 198.
30. Kim RJ, Shah DJ, Judd RM. Erratum: How We Perform Delayed Enhancement Imaging (Journal of Cardiovascular Magnetic Resonance (2003) 5: 3 (505–514)). *Journal of Cardiovascular Magnetic Resonance*. 2003; 5: p. 613–615.
31. Steingoetter A, Menne D, Braren RF. Assessing antiangiogenic therapy response by DCE-MRI: development of a physiology driven multi-compartment model using population pharmacometrics. *PLoS one*. 2011; 6: p. e26366. <https://doi.org/10.1371/journal.pone.0026366> PMID: 22028864
32. Hahn EL. Spin echoes. *Physical review*. 1950; 80: p. 580.
33. Bakker CJG, de Graaf CN, van Dijk P. Derivation of quantitative information in NMR imaging: a phantom study. *Physics in Medicine and Biology*. 1984 December; 29: p. 1511–1525. <https://doi.org/10.1088/0031-9155/29/12/004> PMID: 6514785
34. Sperber GO, Ericsson A, Hemmingsson A, Jung B, Thuomas KÅ. Improved formulae for signal amplitudes in repeated NMR sequences: Applications in NMR imaging. *Magnetic Resonance in Medicine*. 1986 October; 3: p. 685–698. <https://doi.org/10.1002/mrm.1910030505> PMID: 3784887
35. Chavhan GB, Babyn PS, Thomas B, Shroff MM, Haacke EM. Principles, Techniques, and Applications of T2*-based MR Imaging and its Special Applications. *Radiographics*. 2009 September; 29(5): p. 1433–1449. <https://doi.org/10.1148/rg.295095034> PMID: 19755604
36. Croce D, Gucciardo M, Mangione S, Santaromita G, Tinnirello I. Impact of LoRa Imperfect Orthogonality: Analysis of Link-Level Performance. *IEEE Communications Letters*. 2018; 22: p. 796–799.
37. Spadone S, de Pasquale F, Mantini D, Penna SD. A K-means multivariate approach for clustering independent components from magnetoencephalographic data. *NeuroImage*. 2012; 62: p. 1912–1923. <https://doi.org/10.1016/j.neuroimage.2012.05.051> PMID: 22634861
38. de Pasquale F, Spadone S, Betti V, Corbetta M, Penna SD. Temporal modes of hub synchronization at rest. *NeuroImage*. 2021; 235: p. 118005. <https://doi.org/10.1016/j.neuroimage.2021.118005> PMID: 33819608
39. Sinibaldi R, Conti A, Sinjari B, Spadone S, Pecci R, Palombo M, et al. Multimodal-3D imaging based on μ MRI and μ CT techniques bridges the gap with histology in visualization of the bone regeneration process. *Journal of Tissue Engineering and Regenerative Medicine*. 2018; 12: p. 750–761.
40. Varga-Szemes A, Kiss P, Rab A, Suranyi P, Lenkey Z, Simor T, et al. In vitro longitudinal relaxivity profile of Gd (ABE-DTTA), an investigational magnetic resonance imaging contrast agent. *PLoS One*. 2016; 11: p. e0149260. <https://doi.org/10.1371/journal.pone.0149260> PMID: 26872055
41. Clarke J, Hatridge M, Mössle M. SQUID-Detected Magnetic Resonance Imaging in Microtesla Fields. *Annual review of biomedical engineering*. 2007 Feb; 9: p. 389–413. <https://doi.org/10.1146/annurev.bioeng.9.060906.152010> PMID: 17328671
42. Boss MA, Mates JA, Busch SE, SanGiorgio P, Russek SE, Buckenmaier K, et al. Prototype phantoms for characterization of ultralow field magnetic resonance imaging. *Magnetic resonance in medicine*. 2014; 72(6): p. 1793–1800. <https://doi.org/10.1002/mrm.25060> PMID: 24281979
43. Volegov P, Flynn M, Kraus R, Magnelind P, Matlashov A, Nath P, et al. Magnetic Resonance Relaxometry at Low and Ultra Low Fields. In *IFMBE Proceedings*.: Springer Berlin Heidelberg; 2010. p. 82–87.
44. Yin X, Russek S, Zabow G, Sun F, Mohapatra J, Keenan K, et al. Large T1 contrast enhancement using superparamagnetic nanoparticles in ultra-low field MRI. *Scientific Reports*. 2018 August 8; 8: p. 11863. <https://doi.org/10.1038/s41598-018-30264-5> PMID: 30089881